AIAA 2004-3475

Rotational Axisymmetric Mean Flow for the Vortex Injection Hybrid Rocket Engine

J. Majdalani and A. B. Vyas
Advanced Theoretical Research Center
University of Tennessee Space Institute
Tullahoma, TN 37388

40th AIAA/ASME/SAE/ASEE Joint Propulsion Conference and Exhibit
11–14 July 2004
Fort Lauderdale, FL

40th AIAA/ASME/SAE/ASEE Joint Propulsion Conference and Exhibit
11-14 July 2004, Fort Lauderdale, Florida

AIAA 2004-3475

Rotational Axisymmetric Mean Flow for the Vortex Injection Hybrid Rocket Engine

Joseph Majdalani* and Anand B. Vyas†
University of Tennessee Space Institute, Tullahoma, TN 37388

In this work, we derive an approximate solution that describes the mean flow motion of the bidirectional coaxial vortex that characterizes NASA's Hybrid Injection Vortex Rocket Engine (VIHRE). Our mathematical model is based on steady, rotational, axisymmetric, incompressible, and inviscid flow conditions. The resulting Euler-type solution is obtained using variation of parameters; it enables us to reproduce the bipolar motion observed in laboratory-scale VIHRE engines. Other predictions include pressure distributions, axial and radial velocity extrema, vorticity formation, and the dynamic mantle location that separates the outflow from the inflow. By relating fundamental variables to the bidirectional swirl number and wall regression rate, essential flow characteristics are captured. For example, our findings provide an explicit relation between the mantle location and the solid propellant wall regression rate.

Nomenclature

a = chamber radius
A_i = inlet area of the incoming swirl flow
b = chamber discharge radius, βa
l = chamber aspect ratio, L/a
p = normalized pressure, $\overline{p}/(\rho U^2)$
$\overline{Q}_i$ = inlet volumetric flow rate at the base
Q_i = normalized flow rate, $\overline{Q}_i/(Ua^2) = \sigma^{-1}$
Q_{in} = total incoming flow rate, $\overline{Q}_{\text{in}} = \overline{Q}_i + \overline{Q}_w$
$\overline{Q}_w$ = wall-injected flow rate, $2\pi aLU_w$
Re = injection Reynolds number, Ua/ν
r = normalized radial coordinate, $\overline{r}/a$
S = swirl number, $\pi ab/A_i = \pi\beta\sigma$
$\boldsymbol{u}$ = normalized velocity $(\overline{u}_r, \overline{u}_z, \overline{u}_\theta)/U$
U = tangential injection velocity, $\overline{u}_\theta(a, L)$
U_w = wall-injection velocity, $-\overline{u}_r(a, \overline{z}) = \overline{Q}_w/(2\pi aL)$
z = normalized axial coordinate, $\overline{z}/a$

β = normalized discharge radius, b/a
ε = wall-injection parameter, U_w/U
κ = tangential inflow parameter, $(2\pi\sigma l)^{-1}$
$\tilde{\kappa}$ = modified inflow parameter, $\kappa\csc(\pi\beta^2)$
ν = kinematic viscosity, μ/ρ
ρ = density
σ = modified swirl number, $Q_i^{-1} = S/(\pi\beta)$
$\boldsymbol{\Omega}$ = mean flow vorticity, $\nabla\times\boldsymbol{u}$

Subscripts
i = inlet property at the base, $\overline{z} = L$
r = radial component or partial derivative
w = property along the circumferential wall
z = axial component or partial derivative

θ = azimuthal component or partial derivative
= overbars denote dimensional variables

*Jack D. Whitfield Professor of High Speed Flows, Department of Mechanical, Aerospace and Biomedical Engineering. Member AIAA.

†Research Scientist and former Instructor, Marquette University, Department of Mechanical and Industrial Engineering. Member AIAA.

I. Introduction

DUE to recent advancements in propellant composition, injection technology, auxiliary equipment, and chamber design, it may be speculated that the dawn of hybrid rocket commercialization is drawing near. In past years, propulsion industries have refrained from seriously considering hybrid propellants as viable alternatives to liquids or solids because of three principal deficiencies that hybrids have been noted for. These include low combustion efficiency, low regression rate, and low volumetric loading. All three deficiencies may be attributed to the slow diffusion flames that are typically engendered along the interface between solid fuel and gaseous oxidizer. As a result, polymeric fuels used in hybrids are known to display weak burning characteristics as they regress at about an order of magnitude more slowly than solids. To compensate for the low mass flow rate of pyrolyzed fuel, large and expensive pressure cases are required. These cases are needed to hold complex grain shapes that must comprise wide ports and wet surface areas that are sufficiently large to produce the desired thrust distribution. The gist: diffusion flames are no match to

premixed flames unless a mechanism can be conceived to overcome their adverse characteristics.

Despite these long-standing and well-defined setbacks, the three-pronged problem affecting hybrids may not be too difficult to solve. As shown recently by Casillas *et al.*,[1] cost effectiveness of hybrids may be achieved if only a three-to-four fold increase in their fuel regression rate can be accomplished. Such an increase will obviate the need for sophisticated grain designs by promoting major reductions in inert mass.

Bearing these perspectives in mind, an innovative vortex injection hybrid rocket engine (VIHRE) has been recently developed based on a cyclonic flow concept.[2] This engine is expected to find widespread use in both commercial and military applications due to the favorable features that it offers. On advantage of VIHRE is its ability to produce a seven-fold increase in regression-rate by comparison to a classic hybrid.[3-6] According to the criteria furnished by Casillas *et al.*,[1] it provides a feasible propulsion alternative.

The improved performance granted by VIHRE can be attributed to its unique internal flowfield which is dominated by swirling bidirectional motion (see Fig. 1). The corresponding coaxial, counter-flowing vortex pair increases surface erosion while promoting mixing and turbulence.[3-6]

Another feature in VIHRE that constitutes a departure from conventional hybrid conceptualization is the injection of gaseous oxidizer just upstream of the nozzle (between the aft edge of the fuel grain and the inlet to the nozzle). By aligning the injector ports tangentially to the inner circumference, a strong vortex is produced that can travel helically along the fuel grain surface. Fuel particles swept in this manner are compelled to spiral around the chamber axis, thus crossing the chamber length twice before exiting. Naturally, combustion efficiency is considerably improved due to the markedly increased residence time and the intense mixing between fuel and oxidizer. The injected oxidizer is prevented from short-circuiting and draining out the nozzle by the swirl-induced radial pressure gradients that press the incoming stream against the wall circumference; the induced centrifugal forces cause this outer stream to cling to and climb the chamber's cylindrical walls.

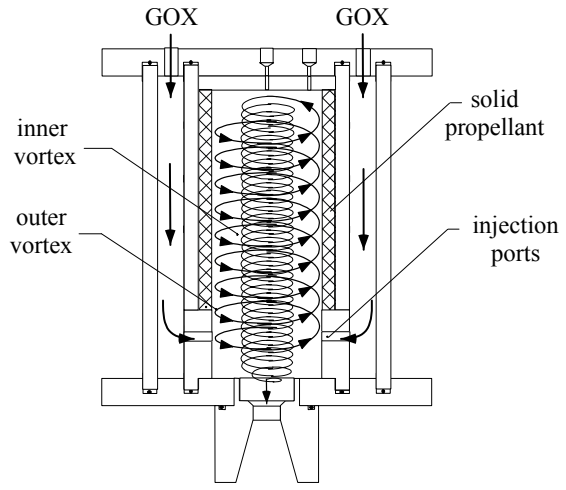

Fig. 1 Schematic of the Vortex Injection Hybrid Rocket Engine (VIHRE) sponsored by NASA.[2]

In addition to the improved regression rate and combustion efficiency, the hybrid vortex engine utilizes a hollow, cylindrical grain cartridge that is simple to mass manufacture. This web perforation shape reduces volumetric loading and precludes the need for large and, therefore, expensive case housing. Another advantage is the increased effective length of the chamber owing to the doubly convoluted path traced by fuel and oxidizer particles. For a given thrust level, the increased effective L^* permits an appreciable reduction in overall length and unused weight.

As in the case of classic hybrids, VIHRE will provide a more reliable alternative than liquid bi-propellants by requiring half of the feed system hardware while providing the same start-stop, mission abort, and throttling capabilities. Furthermore, the non-toxicity of the solid fuel that can be loaded into VIHRE will be less hazardous to store and transport than liquid fuels, less degradable than solids, and more environmentally friendly than either of the two. Due to these safety and operational advantages, the hybrid vortex engine stands to provide an attractive propulsion alternative that combines the advantages of both liquids and solids while reducing their undesirable characteristics.

In this study, the focus will be on providing a closed-form analytical solution that can be used to describe the bulk gas motion observed in an idealized representation of VIHRE. To the authors' knowledge, no analytical solution to model the hybrid vortex has yet been advanced. For this reason, perturbation tools will be employed in conjunction with Euler's equations whose application is justified in view of the large Reynolds numbers that characterize this problem; the goal will be to extract a steady, inviscid, incompressible mean flow approximation for the bidirectional flowfield that arises in the hybrid vortex engine.

II. Mathematical Model

The hybrid vortex engine is modeled as a cylindrical chamber of porous length L and radius a with both a closed head end and a partially open downstream end. The latter is attached to a tubular nozzle of radius b. A sketch of the chamber is given in

Fig. 2 where $\bar{r}$ and $\bar{z}$ are used to denote the radial and axial coordinates. The field of interest stretches from the head end to the base plane in the extent that it remains incompressible. Downstream of the base, the flow is allowed to accelerate by expanding through a nozzle whose analysis falls outside the scope of this study.

At the base, the fraction of the radius that permits an outflow is given by $\beta = b/a$. Along the remaining portion of the base, an incompressible fluid is assumed to enter the chamber tangentially to the inner circumference at a prescribed volumetric rate Q_i. The corresponding tangential injection velocity U is considered to be sufficiently large to mitigate the flow from short-circuiting –a condition by which the flow will drift toward and out of the nozzle. Instead, a bidirectional vortex is formed as in the case of cyclonic separators.[7,8] This bidirectional motion is augmented by a secondary wall influx resulting from the radial and uniformly distributed mass addition originating from the porous circumferential wall. The wall-injection velocity U_w is used to capture the solid propellant regression rate. Clearly, U_w is appreciably smaller than U due to typical rates of fuel pyrolysis. This condition will be exploited in seeking a closed-form asymptotic approximation.

The strong angular momentum born by the incoming stream causes the formation of a cyclone; this phenomenon subdivides the chamber into two vortex zones: an outer annulus that is separated from the inner core region by virtue of a spinning and non-translating cylindrical layer named 'mantle.' In the outer vortex, the spiraling fluid sweeps up the propellant surface while mixing with the wall transpiring mass. At the chamber head end, the outer vortex switches axial polarity, reverses inwardly, and continues spiraling toward and out of the nozzle. The current analysis will seek to capture the essential features of the ensuing flowfield, namely, of the bidirectional vortex in this idealized porous chamber.

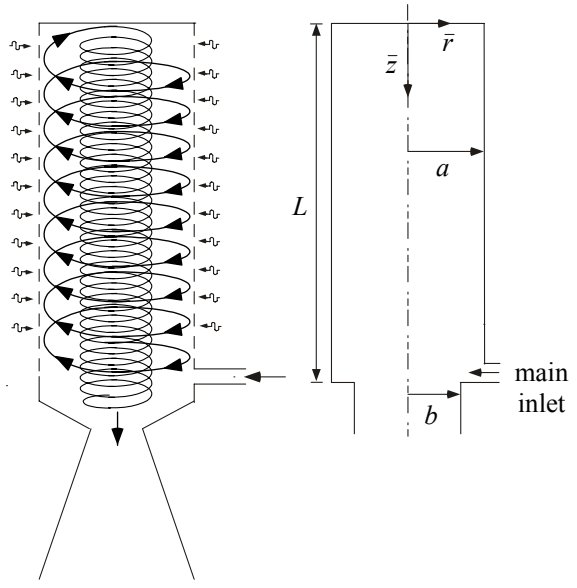

Fig. 2 Sketch of the hybrid vortex chamber noted by the presence of a bidirectional vortex in addition to sidewall mass addition.

A. Equations

In order to characterize the bulk gas motion, a non-reactive-flow model will be used. This may be justified by the weak effects of diffusion flames in typical hybrids. Additionally, the flow will be assumed to be (i) steady, (ii) inviscid, (iii) incompressible, (iv) rotational, and (v) axisymmetric. Axisymmetry is warranted by the strong swirl velocity and the absence of friction to decelerate the flow in the tangential direction. In fact, this assumption recurs so often in the literature that it is generally adopted without scrutiny (see Leibovich[9]). The combination of axisymmetry and frictionless motion leads to another flow attribute of the swirl velocity, namely, axial independence. The weak sensitivity of the swirl velocity to axial variations is corroborated by the work of Leibovich,[9,10] Beran and Culick,[11] Bloor and Ingham,[7,8] Vatistas, Lin and Kwok,[12,13] Szeri and Holmes,[14] and others. Physically, it is granted by the absence of friction between fluid layers and along both the endwall and sidewall. Based on these assumptions, Euler's equations become

$$\frac{1}{\bar{r}}\frac{\partial(\bar{r}\bar{u}_r)}{\partial\bar{r}} + \frac{\partial\bar{u}_z}{\partial\bar{z}} = 0 \tag{1}$$

$$\bar{u}_r\frac{\partial\bar{u}_r}{\partial\bar{r}} + \bar{u}_z\frac{\partial\bar{u}_r}{\partial\bar{z}} - \frac{\bar{u}_\theta^{\,2}}{\bar{r}} = -\frac{1}{\rho}\frac{\partial\bar{p}}{\partial\bar{r}} \tag{2}$$

$$\bar{u}_r\frac{\partial\bar{u}_\theta}{\partial\bar{r}} + \frac{\bar{u}_\theta\bar{u}_r}{\bar{r}} = 0 \tag{3}$$

$$\bar{u}_r\frac{\partial\bar{u}_z}{\partial\bar{r}} + \bar{u}_z\frac{\partial\bar{u}_z}{\partial\bar{z}} = -\frac{1}{\rho}\frac{\partial\bar{p}}{\partial\bar{z}} \tag{4}$$

B. Boundary Conditions

The first set of boundary conditions is due to symmetry and head end impermeability. The second set is due to the inlet configuration and bulk mass conservation. Specifically, one can assume

(a) a fully tangential inflow,
(b) a zero axial flow at the head end,
(c) symmetry about the centerline,
(d) a prescribed radial inflow at the sidewall, and
(e) an inflow that matches the outflow at the base.

These particular conditions translate into

$$\begin{cases} \bar{r}=a,\ \bar{z}=L,\ \bar{u}_\theta = U \text{ (tangential injection)} \\ \bar{z}=0,\ \forall \bar{r},\ \bar{u}_z = 0 \text{ (inert head end)} \\ \bar{r}=0,\ \forall \bar{z},\ \bar{u}_r = 0 \text{ (axisymmetry)} \\ \bar{r}=a,\ 0 \le \bar{z} < L,\ \bar{u}_r = -U_w \text{ (sidewall injection)} \\ \bar{z}=L,\ 0 \le \bar{r} < b,\ \bar{Q}_i = UA_i \text{ (inflow at the base)} \end{cases} \quad (5)$$

C. Normalization

In seeking a similarity solution, it is helpful to normalize the principal variables and/or operators. This can be accomplished by setting

$$z = \frac{\bar{z}}{a};\ r = \frac{\bar{r}}{a};\ \nabla = a\bar{\nabla};\ \ \beta = \frac{b}{a} \quad (6)$$

$$u_r = \frac{\bar{u}_r}{U};\ u_\theta = \frac{\bar{u}_\theta}{U};\ u_z = \frac{\bar{u}_z}{U};\ \ \varepsilon = \frac{U_w}{U} \quad (7)$$

$$p = \frac{\bar{p}}{\rho U^2};\ Q_i = \frac{\bar{Q}_i}{Ua^2} = \frac{A_i}{a^2};\ Q_w = \frac{\bar{Q}_w}{Ua^2} = 2\pi\varepsilon l \quad (8)$$

Here $U = \bar{u}_\theta(a, L)$ and $U_w = -\bar{u}_r(a, \bar{z})$ represent the average fluid injection velocity at the base and the uniform wall-injection velocity along the sidewall, respectively.

At this juncture, it may be instructive to mark the relation that exists between the normalized volumetric flow rate Q_i and the swirl number S used in the literature.[15] In many studies such as the one by Hoekstra, Derksen and Van den Akker,[16] the swirl number for cyclonic flow is presented by

$$S \equiv \pi ab / A_i = \pi\beta\sigma \quad (9)$$

where $\sigma \equiv Q_i^{-1}$ is used to refer to the modified swirl number that appears in this study. Clearly, $\sigma \equiv Q_i^{-1}$ is directly proportional to the classic swirl number.

Pursuant to Eqs. (6)–(8), rotational axisymmetric mean flow motion is prescribed by

$$\nabla \cdot \boldsymbol{u} = 0\ ; \qquad \boldsymbol{u} \cdot \nabla \boldsymbol{u} = -\nabla p \quad (10)$$

After substituting $\boldsymbol{u} \cdot \nabla \boldsymbol{u} = \frac{1}{2}\nabla(\boldsymbol{u} \cdot \boldsymbol{u}) - \boldsymbol{u} \times \nabla \times \boldsymbol{u}$ into Eq. (10), one can take the curl of the momentum equation to obtain, as usual, the steady and inviscid vorticity transport equation:

$$\nabla \times \boldsymbol{u} \times \boldsymbol{\Omega} = 0\ ; \quad \boldsymbol{\Omega} \equiv \nabla \times \boldsymbol{u} \quad (11)$$

The corresponding boundary conditions become

$$\begin{cases} u_\theta(1, l) = 1;\ \ u_z(r, 0) = 0;\ \ u_r(1, z) = -\varepsilon \\ u_r(0, z) = 0;\ Q_{\text{out}} = \int_0^{2\pi}\int_0^{\beta} \boldsymbol{u}(r, l) \cdot \hat{\boldsymbol{n}}\, r\, \mathrm{d}r\mathrm{d}\theta = Q_{\text{in}} \end{cases} \quad (12)$$

where $\boldsymbol{u} \cdot \hat{\boldsymbol{n}} = u_z$ represents the outflow velocity at the base while $Q_{\text{in}} = Q_i + Q_w$ accounts for the injected flow at the base augmented by the wall-injected fluid.

The presence of a small parameter ε in Eq. (12) suggests the possibility of an asymptotic treatment. Specifically, a regular perturbation expansion may be applied to the velocity and its accompanying vorticity. This can be implemented by letting

$$\boldsymbol{u} = \boldsymbol{u}^{(0)} + \varepsilon \boldsymbol{u}^{(1)} + O(\varepsilon^2)\ ; \boldsymbol{\Omega} = \boldsymbol{\Omega}^{(0)} + \varepsilon \boldsymbol{\Omega}^{(1)} + O(\varepsilon^2) \quad (13)$$

These expressions can be substituted into Eq. (11). The perturbed vorticity transport equation yields

$$\nabla \times \boldsymbol{u}^{(0)} \times \boldsymbol{\Omega}^{(0)} + \varepsilon \nabla \times \boldsymbol{u}^{(1)} \times \boldsymbol{\Omega}^{(0)} + \varepsilon \nabla \times \boldsymbol{u}^{(0)} \times \boldsymbol{\Omega}^{(1)} + \varepsilon^2 \nabla \times \boldsymbol{u}^{(1)} \times \boldsymbol{\Omega}^{(1)} = 0 \quad (14)$$

The solution to this set will be described next.

III. Solution

Before carrying out the asymptotic treatment, it may be helpful to consider the state of the swirl velocity in light of the foregoing assumptions. Specifically, it may be useful to show that, at leading order, the swirl velocity decouples from the momentum equation and reduces the complexity of Eqs. (13)–(14).

A. A Free Outer Vortex

From the θ – momentum equation given by Eq. (3) one can put

$$u_r \left(\frac{\partial u_\theta}{\partial r} + \frac{u_\theta}{r} \right) = 0 \quad (15)$$

where $u_\theta(1, l) = 1$. Subsequently, one finds

$$u_\theta = 1/r \quad (16)$$

As usual, Eq. (16) confirms the presence of a free vortex motion that is characteristic of swirling inviscid flow. Hence, at leading order, both radial and axial components of vorticity vanish identically.

B. Leading-Order Approximation

At this juncture, both radial and axial velocity components remain to be determined from the reduced set given by

$$\frac{1}{r}\frac{\partial [r u_r^{(0)}]}{\partial r} + \frac{\partial u_z^{(0)}}{\partial z} = 0 \text{ (continuity)} \quad (17)$$

$$\frac{\partial [u_r^{(0)} \Omega_\theta^{(0)}]}{\partial r} + \frac{\partial [u_z^{(0)} \Omega_\theta^{(0)}]}{\partial z} = 0 \text{ (vorticity transport)} \quad (18)$$

$$\frac{\partial u_r^{(0)}}{\partial z} - \frac{\partial u_z^{(0)}}{\partial r} = \Omega_\theta^{(0)} \text{ (vorticity)} \quad (19)$$

Realizing that the swirl velocity is decoupled from the remaining set, the introduction of the Stokes streamfunction appears to be a possibility despite the overall three-dimensionality of the velocity field. As usual, the Stokes streamfunction ψ in cylindrical coordinates can be expressed by

$$u_r^{(0)} = -\frac{1}{r}\frac{\partial \psi^{(0)}}{\partial z}; \quad u_z^{(0)} = \frac{1}{r}\frac{\partial \psi^{(0)}}{\partial r}; \tag{20}$$

where $\psi = \psi^{(0)} + \varepsilon\psi^{(1)} + O(\varepsilon^2)$ is a series of diminishing terms. When this transformation is used in the vorticity transport equation given by Eq. (18), one obtains, at leading order,

$$-\frac{\partial \psi^{(0)}}{\partial z}\frac{\partial}{\partial r}\left[\frac{\Omega_\theta^{(0)}}{r}\right] + \frac{\partial \psi^{(0)}}{\partial r}\frac{\partial}{\partial z}\left[\frac{\Omega_\theta^{(0)}}{r}\right] = 0 \tag{21}$$

and so

$$\frac{\left[\Omega_\theta^{(0)}/r\right]_z}{\left[\Omega_\theta^{(0)}/r\right]_r} = \frac{\left[\psi^{(0)}\right]_z}{\left[\psi^{(0)}\right]_r} \tag{22}$$

The resulting equality will hold if, and only if,

$$\Omega_\theta^{(0)} = rF[\psi^{(0)}(r,z)] \tag{23}$$

When this standard form is substituted into Eq. (22), it can be promptly seen that

$$\frac{\left[\Omega_\theta^{(0)}/r\right]_z}{\left[\Omega_\theta^{(0)}/r\right]_r} = \frac{\left\{F[\psi^{(0)}]\right\}_z}{\left\{F[\psi^{(0)}]\right\}_r} = \frac{F_{\psi^{(0)}}[\psi^{(0)}]_z}{F_{\psi^{(0)}}[\psi^{(0)}]_r} = \frac{[\psi^{(0)}]_z}{[\psi^{(0)}]_r} \tag{24}$$

According to Eq. (23), F can be a general function of $\psi^{(0)}$. The two simplest cases correspond to $F = C^2$ and $F = C^2\psi^{(0)}$, where C is some constant. While it is a trivial exercise to prove that the first form is incongruent with the boundary conditions, the linear relationship, on the other hand, can be shown to be suitable. At the outset, one can put

$$\Omega_\theta^{(0)} = C^2 r\psi^{(0)} \tag{25}$$

It must be born in mind that this linear choice may not be unique although the authors have been unable to identify other alternatives that can yield a closed-form solution. When Eq. (25) is inserted into the vorticity equation one obtains the classic result[17]

$$\frac{\partial^2 \psi^{(0)}}{\partial z^2} + \frac{\partial^2 \psi^{(0)}}{\partial r^2} - \frac{1}{r}\frac{\partial \psi^{(0)}}{\partial r} + C^2 r^2 \psi^{(0)} = 0 \tag{26}$$

At this point, three of the boundary conditions may be written for the streamfunction. Based on Eq. (12), one has

$$\begin{cases} z = 0; \;\; u_z^{(0)} = 0; \;\; \partial\psi^{(0)}/\partial r = 0 \\ r = 0; \;\; u_r^{(0)} = 0; \;\; \partial\psi^{(0)}/\partial z = 0 \\ r = 1; \;\; u_r^{(0)} = 0; \;\; \partial\psi^{(0)}/\partial z = 0 \end{cases} \tag{27}$$

It must be noted that the set given by Eqs. (26)–(27) has already been solved (exactly) by Vyas, Majdalani and Chiaverini[18] in the context of a bidirectional vortex in a liquid rocket engine. Without further ado, the corresponding solution is reproduced here to the extent that it constitutes the leading-order expansion for the hybrid vortex as well. Using the present nomenclature, one finds

$$\psi^{(0)} = B\, z \sin(\pi r^2) \tag{28}$$

The velocity field corresponding to Eq. (28) becomes

$$\boldsymbol{u}^{(0)} = -\frac{B}{r}\sin(\pi r^2)\boldsymbol{e}_r + \frac{1}{r}\boldsymbol{e}_\theta + 2B\pi z\cos(\pi r^2)\boldsymbol{e}_z \tag{29}$$

In order to calculate the last constant, global mass balance must be carefully applied to account for the radial inflow along the sidewall. Given that

$$Q_{\text{in}} = Q_{\text{out}} = Q_i + Q_w \tag{30}$$

one can calculate

$$Q_i = \frac{A_i}{a^2} \;\text{ and }\; Q_w = \frac{U_w(2\pi aL)}{Ua^2} = 2\pi\varepsilon l \tag{31}$$

to obtain

$$Q_{\text{in}} = Q_i + Q_w = \frac{A_i}{a^2} + 2\pi\varepsilon l = Q_{\text{out}} \tag{32}$$

At leading order ($\varepsilon = 0$), mass conservation requires that

$$2\pi\int_0^\beta \boldsymbol{u}^{(0)}\cdot\hat{\boldsymbol{n}}\; r\mathrm{d}r = 2\pi\int_0^\beta u_z^{(0)} r\mathrm{d}r = Q_i \tag{33}$$

and so

$$B = Q_i \csc(\pi\beta^2)/(2\pi l) \tag{34}$$

It follows that the leading-order velocity field may be expressed by

$$\boldsymbol{u}^{(0)} = -\frac{Q_i \sin(\pi r^2)}{2\pi l \sin(\pi\beta^2) r}\boldsymbol{e}_r + \frac{1}{r}\boldsymbol{e}_\theta + \frac{Q_i z}{l\sin(\pi\beta^2)}\cos(\pi r^2)\boldsymbol{e}_z \tag{35}$$

Thus, by letting

$$\tilde{\kappa} \equiv \frac{Q_i}{2\pi l \sin(\pi\beta^2)} = \kappa\csc(\pi\beta^2) \tag{36}$$

one can put

$$\psi^{(0)} = \tilde{\kappa} z \sin(\pi r^2) \tag{37}$$

$$\Omega_\theta^{(0)} = 4\pi^2\tilde{\kappa} r z \sin(\pi r^2) \tag{38}$$

and

$$\boldsymbol{u}^{(0)} = -\frac{\tilde{\kappa}}{r}\sin(\pi r^2)\boldsymbol{e}_r + \frac{1}{r}\boldsymbol{e}_\theta + 2\pi\tilde{\kappa} z\cos(\pi r^2)\boldsymbol{e}_z \tag{39}$$

Other important flow characteristics at leading order include

$$\frac{\partial p^{(0)}}{\partial r} = \frac{1 + \tilde{\kappa}^2\left[\sin^2(\pi r^2) - \pi r^2\sin(2\pi r^2)\right]}{r^3} \tag{40}$$

$$\frac{\partial p^{(0)}}{\partial z} = -4\pi^2\tilde{\kappa}^2 z \tag{41}$$

and

$$\Delta p^{(0)} = -\frac{1}{2r^2}\left\{1+\tfrac{1}{2}\tilde{\kappa}^2\left[8\pi^2 r^2 z^2 + 1 - \cos(2\pi r^2)\right]\right\} \tag{42}$$

C. First-Order Equation with Wall Injection

Before setting up the first-order solution, it must be noted that the swirl velocity is not perturbed and, as such, the angular momentum equation remains uncoupled from the axial and radial momentum equations at all orders. At $O(\varepsilon)$, the perturbed mass conservation and vorticity transport equations appear as

$$\nabla\cdot\boldsymbol{u}^{(1)} = 0\,;\ \nabla\times\boldsymbol{u}^{(1)}\times\boldsymbol{\Omega}^{(0)} + \nabla\times\boldsymbol{u}^{(0)}\times\boldsymbol{\Omega}^{(1)} = 0 \tag{43}$$

The corresponding boundary conditions become

$$\begin{cases} u_z^{(1)}(r,0) = 0\,;\ \ u_r^{(1)}(1,z) = -1 \\ u_r^{(1)}(0,z) = 0;\ Q_w = \int_0^{2\pi}\int_0^{\beta} \boldsymbol{u}^{(1)}(r,l)\cdot\hat{\boldsymbol{n}}\; r\,\mathrm{d}r\,\mathrm{d}\theta \end{cases} \tag{44}$$

As before, one may let

$$\boldsymbol{u}^{(1)} = -\frac{1}{r}\frac{\partial\psi^{(1)}}{\partial z}\boldsymbol{e}_r + \frac{1}{r}\frac{\partial\psi^{(1)}}{\partial r}\boldsymbol{e}_z \tag{45}$$

At $O(\varepsilon)$, the first and second terms in the linearized vorticity transport equation give

$$\nabla\times\boldsymbol{u}^{(0)}\times\boldsymbol{\Omega}^{(1)} = -\left\{\frac{\partial[u_r^{(0)}\Omega_\theta^{(1)}]}{\partial r} + \frac{\partial(u_z^{(0)}\Omega_\theta^{(1)})}{\partial z}\right\}\boldsymbol{e}_\theta \tag{46}$$

and

$$\nabla\times\boldsymbol{u}^{(1)}\times\boldsymbol{\Omega}^{(0)} = -\left\{\frac{\partial[u_r^{(1)}\Omega_\theta^{(0)}]}{\partial r} + \frac{\partial[u_z^{(1)}\Omega_\theta^{(0)}]}{\partial z}\right\}\boldsymbol{e}_\theta \tag{47}$$

Substituting Eqs. (46)–(47) into the linearized vorticity transport equation given by Eq. (43) leads to

$$\frac{\partial}{\partial r}\left[u_r^{(0)}\Omega_\theta^{(1)} + u_r^{(1)}\Omega_\theta^{(0)}\right] + \frac{\partial}{\partial z}\left[u_z^{(0)}\Omega_\theta^{(1)} + u_z^{(1)}\Omega_\theta^{(0)}\right] = 0 \tag{48}$$

where

$$\Omega_\theta^{(1)} = \frac{\partial u_r^{(1)}}{\partial z} - \frac{\partial u_z^{(1)}}{\partial r} = \frac{\partial}{\partial z}\left[-\frac{1}{r}\frac{\partial\psi^{(1)}}{\partial z}\right] - \frac{\partial}{\partial r}\left[\frac{1}{r}\frac{\partial\psi^{(1)}}{\partial r}\right] \tag{49}$$

To be consistent with the similarity transformation of the velocity at the zeroth order, the radial velocity must be taken to be dependent on the radial coordinate only. On the one hand, this requires a streamfunction of the form $\psi^{(1)} = z\,f(r)$. On the other hand, one may let $u_r^{(1)} = u_r^{(1)}(r)$ so that Eq. (49) reduces to

$$\Omega_\theta^{(1)} = -\frac{\partial u_z^{(1)}}{\partial r} = -\frac{\partial}{\partial r}\left[\frac{1}{r}\frac{\partial\psi^{(1)}}{\partial r}\right] \tag{50}$$

After inserting $\psi^{(1)} = z\,f(r)$ and Eqs. (39)–(50) into Eq. (48), one obtains

$$\frac{1}{r}\frac{\mathrm{d}}{\mathrm{d}r}\left[\frac{\sin(\pi r^2)}{r}\frac{\mathrm{d}}{\mathrm{d}r}\left(\frac{1}{r}\frac{\mathrm{d}f}{\mathrm{d}r}\right) - 4\pi^2\sin(\pi r^2)f\right]$$
$$-4\pi\cos(\pi r^2)\frac{1}{r}\frac{\mathrm{d}}{\mathrm{d}r}\left(\frac{1}{r}\frac{\mathrm{d}f}{\mathrm{d}r}\right) + 8\pi^2\frac{1}{r}\frac{\mathrm{d}f}{\mathrm{d}r}\sin(\pi r^2) = 0 \tag{51}$$

It is now appropriate to employ $\eta \equiv \frac{1}{2}r^2$. After some algebra, Eq. (51) collapses into

$$\sin(2\pi\eta)\frac{\mathrm{d}^3 f}{\mathrm{d}\eta^3} - 2\pi\cos(2\pi\eta)\frac{\mathrm{d}^2 f}{\mathrm{d}\eta^2}$$
$$+4\pi^2\sin(2\pi\eta)\frac{\mathrm{d}f}{\mathrm{d}\eta} - 8\pi^3\cos(2\pi\eta)f = 0 \tag{52}$$

D. Solution by Variation of Parameters

Following Majdalani, Vyas and Flandro,[19] one solution to Eq. (52) may be guessed to be $f(\eta) = C\sin(2\pi\eta)$. Using the method of variation of parameters (see Zhou and Majdalani[20]) the total solution $f(\eta)$ may be compiled by allowing C to vary. Starting with the derivatives,

$$\frac{\mathrm{d}f}{\mathrm{d}\eta} = \sin(2\pi\eta)C' + 2\pi\cos(2\pi\eta)C \tag{53}$$

$$\frac{\mathrm{d}^2 f}{\mathrm{d}\eta^2} = \sin(2\pi\eta)C'' + 4\pi\cos(2\pi\eta)C' - 4\pi^2\sin(2\pi\eta)C \tag{54}$$

and

$$\frac{\mathrm{d}^3 f}{\mathrm{d}\eta^3} = \sin(2\pi\eta)C''' + 6\pi\cos(2\pi\eta)C''$$
$$-12\pi^2\sin(2\pi\eta)C' - 8\pi^3\cos(2\pi\eta)C \tag{55}$$

one may substitute Eqs. (53)–(55) into Eq. (52); many terms cancel out to the extent that one is left with

$$\sin^2(2\pi\eta)C''' + 2\pi\sin(4\pi\eta)C'' - 8\pi^2 C' = 0 \tag{56}$$

Equation (56) can be readily solved using a symbolic computation software;[21] the result is

$$C(\eta) = C_1 - \tfrac{1}{4}\left(C_2\eta + 2C_3\right)\cot(2\pi\eta)/\pi \tag{57}$$

where C_1, C_2, and C_3 are pure constants. Recalling that $f(\eta) = C(\eta)\sin(2\pi\eta)$, one can put

$$f = C_1\sin(2\pi\eta) - \tfrac{1}{4}\left(C_2\eta + 2C_3\right)\cos(2\pi\eta)/\pi \tag{58}$$

Reverting back to the radial coordinate, the total solution may be represented by

$$f(r) = C_1\sin(\pi r^2) - C_6 r^2\cos(\pi r^2) - C_5\cos(\pi r^2) \tag{59}$$

and so

$$\psi^{(1)} = C_1 z \sin(\pi r^2) - C_6 z r^2 \cos(\pi r^2) - C_5 z \cos(\pi r^2) \quad (60)$$

At length, one finds

$$u_r^{(1)} = -\frac{C_1}{r}\sin(\pi r^2) + C_6 r \cos(\pi r^2) + C_5 \frac{\cos(\pi r^2)}{r} \quad (61)$$

To observe the underlying assumption of axisymmetry, C_5 must vanish. Moreover, to comply with the wall-injection boundary condition in Eq. (44), C_6 must be unity. It must be realized that the hard-wall boundary condition at the head end is automatically satisfied –having employed the proper ansatz, $\psi^{(1)} = z\, f(r)$. Only one constant remains at large, namely, C_1. The remaining axial term becomes

$$u_z^{(1)} = 2\pi C_1 z \cos(\pi r^2) - 2z\cos(\pi r^2) + 2\pi z r^2 \sin(\pi r^2) \quad (62)$$

The last constant C_1 may be determined from the global mass balance at the first order. Starting with

$$Q_w = 2\pi l = 2\pi \int_0^{\beta} u_z^{(1)}(r,l)\, r\, \mathrm{d}r \quad (63)$$

one finds $C_1 = [1+\beta^2\cos(\pi\beta^2)]\csc(\pi\beta^2)$. Forthwith, the first-order streamfunction and its velocity components may be updated, namely,

$$\psi^{(1)} = [1+\beta^2\cos(\pi\beta^2)]\csc(\pi\beta^2)\, z\sin(\pi r^2) - z r^2 \cos(\pi r^2) \quad (64)$$

$$u_r^{(1)} = -[1+\beta^2\cos(\pi\beta^2)]\csc(\pi\beta^2)\sin(\pi r^2)/r + r\cos(\pi r^2) \quad (65)$$

and

$$u_z^{(1)} = 2\pi[1+\beta^2\cos(\pi\beta^2)]\csc(\pi\beta^2) z\cos(\pi r^2) - 2z\cos(\pi r^2) + 2\pi z r^2 \sin(\pi r^2) \quad (66)$$

IV. Results and Discussion

A. Wall-Injection Velocity Estimates

The wall-injection velocity may be estimated from experiments yielding correlations for r_s, the solid fuel regression rate.[3] The estimates are generally based on the assumption of steady state regression of propellant grain. To that end, one must recall that simple mass conservation along the pyrolyzing surface of the regressing grain requires that

$$\rho_s r_s = \rho_g U_w \quad (67)$$

where subscripts *s* and *g* refer to the solid and gas phases, respectively. The gas density at the regressing surface may be estimated using the ideal gas equation of state. Based on empirical studies by Chiaverini and co-workers,[22] the average surface temperature may be taken to be 1000 K. The solid phase may be specified to be, for example, HTPB fuel, and the corresponding density may be found accordingly. In the same vein, the regression rate, r_s, may be obtained from available literature.[3]

For the typical hybrid vortex, the wall-injection velocity U_w may vary between 0.3 and 2.5 m/s while the average oxidizer injection velocity U is held at 260 m/s. The wall-injection parameter ε can hence vary between 0.001 and 0.01.

B. Mantle Sensitivity to Wall Injection

Being the fluid layer that separates the outer vortex from the inner one, the so-called mantle (or spinning wheel) is allowed to rotate but not to translate. Being defined by the surface along which the axial velocity vanishes, the mantle can be located by solving

$$u_z = u_z^{(0)} + \varepsilon u_z^{(1)} = 0 \quad (68)$$

and so

$$2z\cos(\pi r^2)\{\pi\tilde{\kappa} + \pi\varepsilon[1+\beta^2\cos(\pi\beta^2)]\csc(\pi\beta^2) - \varepsilon\} + 2\pi\varepsilon z r^2 \sin(\pi r^2) = 0 \quad (69)$$

Using $r = \beta^*$ to denote the radius of the mantle, this root can be determined from Eq. (69) for an arbitrary chamber opening β. We are especially interested in the ideal flow that can be achieved when the nozzle radius is coincident with the mantle radius. Thus, by setting $\beta = \beta^*$, the radius of the inner vortex (exiting the chamber) will match the radius of the chamber opening. This ideal condition will lead to a smooth outflow, mitigating the formation of corner vortices that could otherwise arise from wall collisions along the exit plane. Granted this idealization, Eq. (69) reduces to

$$2z\cos(\pi\beta^{*2})\{\pi\tilde{\kappa} + \pi\varepsilon[1+\beta^{*2}\cos(\pi\beta^{*2})]\csc(\pi\beta^{*2}) - \varepsilon\} + 2\pi\varepsilon z\beta^{*2}\sin(\pi\beta^{*2}) = 0 \quad (70)$$

For $\kappa = 0.01$ and $\varepsilon = 0.001$ the mantle location obtained via Eq. (70) is 0.717888. Increasing the wall injection to $\varepsilon = 0.005$ moves the mantle closer to the wall as β^* shifts to 0.753472.

Explicit roots may be obtained asymptotically using a quadratic polynomial spun off Taylor's series of Eq. (70) about the point $\beta^* = 1/\sqrt{2}$; this particular root corresponds to the limiting physical process for which the solution approaches the case of insignificant injection ($\varepsilon \to 0$). After some algebra, one gets

$$\beta^* = (A - \sqrt{C})/B \quad (71)$$

where

$$\begin{cases} A = \pi^2\varepsilon/\sqrt{2}; \quad B = 4\varepsilon - 2\pi\varepsilon + \pi^2\varepsilon - 2\pi\kappa \\ C = 4\varepsilon^2 - 6\pi\varepsilon^2 + \pi^2\varepsilon^2 - 6\pi\varepsilon\kappa + 4\pi^2\varepsilon\kappa + 2\pi^2\kappa^2 \end{cases} \quad (72)$$

The roots determined using Eq. (71) are 0.717896, 0.754199, and 0.790398 corresponding to $\kappa = 0.01$ and ε values of 0.001, 0.005 and 0.01, respectively.

Unsurprisingly, both the swirl parameter κ and the wall-injection parameter ε affect the mantle location β^*. This is contrary to the behavior observed in the case of bidirectional flow in an idealized liquid rocket engine.[18]

In order to assess the mantle sensitivity to wall injection, ε can be varied at constant κ or vice versa. Results are shown in Table 1 where κ is held at 0.01 while ε is varied from 0 to 0.01. Note that at $\varepsilon = 0$ the case for the liquid vortex engine is recovered. When wall injection is increased, the mantle is pushed closer to the sidewall; this trend can be attributed to the increased secondary mass flowing into the inner vortex at higher regression rates; the increased mass flux causes the inner vortex to expand by pressing the outer annular region against the sidewall.

C. Streamlines

In order to better visualize the bidirectional flowfield, streamlines are plotted in Fig. 3 for $\kappa = 0.01$ and an order of magnitude increase in wall injection. For steady flow, one recalls that streamlines, pathlines, and streaklines coincide in describing the trajectory of fluid particles throughout the chamber. These plots confirm that the mantle location does not vary in the axial direction and that the turning point in the axial velocity approaches the sidewall at higher values of ε. The full asymptotic expression for ψ may be written as

$$\psi = \psi^{(0)} + \varepsilon\psi^{(1)} + O(\varepsilon^2)$$
$$= \kappa \csc(\pi\beta^2)\, z \sin(\pi r^2) + \varepsilon\{[1 + \beta^2 \cos(\pi\beta^2)]$$
$$\times \csc(\pi\beta^2) z \sin(\pi r^2) - z r^2 \cos(\pi r^2)\} + O(\varepsilon^2) \quad (73)$$

D. Axial Velocity Distribution

The axial velocity is described in Fig. 4. There it can be seen that as ε is increased from 0 to 0.01, the centerline velocity is nearly doubled. This appreciable velocity increase can be once more attributed to the role of sidewall mass injection; in this case, it causes the axial velocity magnitude to increase throughout the inner vortex, a trend that supports the streamline behavior described earlier. The total axial velocity can be expressed as

$$u_z = u_z^{(0)} + \varepsilon u_z^{(1)} + O(\varepsilon^2)$$
$$= \{\pi\kappa \csc(\pi\beta^2) + \pi\varepsilon[1 + \beta^2 \cos(\pi\beta^2)]\csc(\pi\beta^2) - \varepsilon\}$$
$$\times 2z\cos(\pi r^2) + 2\pi\varepsilon z r^2 \sin(\pi r^2) + O(\varepsilon^2) \quad (74)$$

Table 1 Mantle location

No.	κ	ε	β^*	$\beta^* - 1/\sqrt{2}$
1	0.01	0.000	0.707	0.000
2	0.01	0.001	0.718	0.011
3	0.01	0.005	0.752	0.045
4	0.01	0.010	0.786	0.079

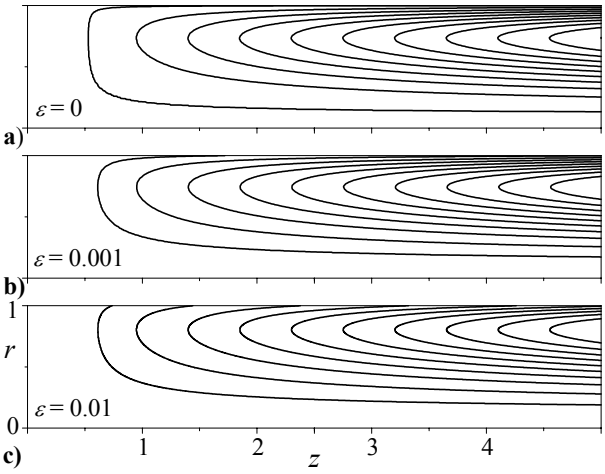

Fig. 3 Swirling bidirectional flow streamlines with increasing sidewall injection. Here $\kappa = 0.01$.

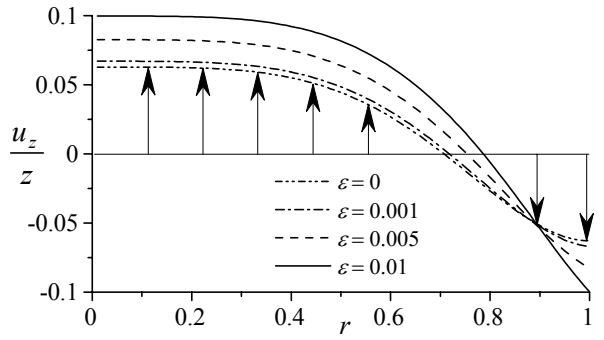

Fig. 4 Axial velocity distribution for $\kappa = 0.01$ and several wall injection rates.

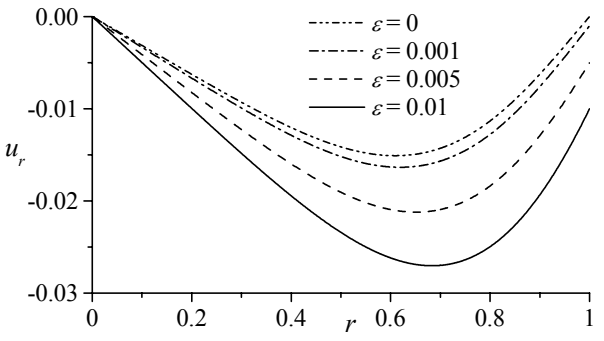

Fig. 5 Radial velocity distribution for $\kappa = 0.01$ and several wall injection rates.

E. Radial Velocity Distribution

The radial velocity is illustrated in Fig. 5 for $\kappa = 0.01$ and the usual values of the perturbation parameter. It is interesting to note the shift in maximum u_r in the direction of the wall with successive increases in sidewall mass addition. This trend is consistent with the movement of the mantle. The radial velocity for the hybrid model may be expressed by

$$u_r = u_r^{(0)} + \varepsilon u_r^{(1)} + O(\varepsilon^2)$$
$$= -\kappa \csc(\pi\beta^2) r^{-1} \sin(\pi r^2) - \varepsilon \left\{ r^{-1} \sin(\pi r^2) \csc(\pi\beta^2) \right.$$
$$\left. \times [1 + \beta^2 \cos(\pi\beta^2)] - r \cos(\pi r^2) \right\} + O(\varepsilon^2) \qquad (75)$$

To accurately predict the maximum radial velocity and its locus, one can set $\mathrm{d}u_r / \mathrm{d}r = 0$ and solve for $r = r_m$. The outcome is

$$\kappa \csc(\pi\beta^2) \sin(\pi r_m^2) - 2\pi\kappa r_m^2 \csc(\pi\beta^2) \cos(\pi r_m^2)$$
$$+ \varepsilon [r_m^2 \cos(\pi r_m^2) - 2\pi\beta^2 \cot(\pi\beta^2) r_m^2 \cos(\pi r_m^2)$$
$$-2\pi \csc(\pi\beta^2) r_m^2 \cos(\pi r_m^2) - 2\pi r_m^4 \sin(\pi r_m^2)$$
$$+ \beta^2 \cot(\pi\beta^2) \sin(\pi r_m^2) + \csc(\pi\beta^2) \sin(\pi r_m^2)] = 0 \qquad (76)$$

Considering the transcendental nature of Eq. (76), a numerical root finding technique may be employed. Results are sketched in Table 2 where κ is kept fixed while ε is varied. One finds that the radial velocity maxima occur at the normalized radius of 0.61, 0.62, 0.65, and 0.68 for $\varepsilon = 0$, 0.001, 0.005, and 0.01, respectively. At these locations, $|(u_r)_{\max}|$ is rendered equal to 0.015, 0.016, 0.021 and 0.027, respectively.

Alternatively, an asymptotic expression for the radial velocity maximum and its location can also be determined using the same series expansion approach attempted for the mantle location. One finds

$$r_m = (A - \sqrt{C}) / B \qquad (77)$$

where

$$A = \sqrt{2} \begin{bmatrix} -\pi^3\varepsilon - \cot(\pi\beta^2)\left(16\varepsilon\beta^2 - 2\varepsilon\beta^2\pi^2\right) \\ +\csc(\pi\beta^2)\left(16\varepsilon + 2\pi^2\varepsilon - 16\kappa - 2\pi^2\kappa\right) \end{bmatrix} \qquad (78)$$

Table 2 Radial velocity maxima

No.	κ	ε	$r_{\max}$	$(u_r)_{\max}$
1	0.01	0.000	0.609	-0.015
2	0.01	0.001	0.618	-0.016
3	0.01	0.005	0.650	-0.021
4	0.01	0.010	0.683	-0.027

$$B = \begin{bmatrix} 6\pi\varepsilon - 2\pi^3\varepsilon - 24\beta^2\varepsilon \cot(\pi\beta^2) \\ -24 \csc(\pi\beta^2)(\varepsilon + \kappa) \end{bmatrix} \qquad (79)$$

$$C = A^2 - \begin{bmatrix} 6\pi\varepsilon + 2\pi^3\varepsilon + 24\beta^2\varepsilon \cot(\pi\beta^2) \\ +24 \csc(\pi\beta^2)(\varepsilon + \kappa) \end{bmatrix}$$
$$\times \begin{bmatrix} \pi\varepsilon + \pi^3\varepsilon + \cot(\pi\beta^2)\left(24\beta^2\varepsilon - 4\pi^2\beta^2\right) \\ +\csc(\pi\beta^2)\left(24\varepsilon - 4\pi^2\varepsilon + 24\kappa - 4\pi^2\kappa\right) \end{bmatrix} \qquad (80)$$

The radial velocity maxima for ε values of 0.001, 0.005 and 0.01 are located at 0.620972, 0.651096, and 0.68322, respectively. The corresponding maximum radial velocities are determined as -0.016346, -0.021214, and -0.027028, respectively.

F. Pressure Distributions

The pressure gradients in the radial and axial directions can be determined using Eqs. (10), (13), (39), (65) and (66); after some algebra, one finds

$$\frac{\partial p}{\partial r} = \frac{1 + \kappa^2 \csc^2(\pi\beta^2)[\sin^2(\pi r^2) - \pi r^2 \sin(2\pi r^2)]}{r^3}$$
$$+ \varepsilon \frac{2\kappa \csc(\pi\beta^2)}{r^3} \{[-\pi r^4 + \beta^2 \cot(\pi\beta^2) + \csc(\pi\beta^2)]$$
$$\times \sin^2(\pi r^2) + \pi r^4 \cos^2(\pi r^2)$$
$$-\pi r^2 [\beta^2 \cot(\pi\beta^2) + \csc(\pi\beta^2)] \sin(2\pi r^2)\} \qquad (81)$$

and

$$\frac{\partial p}{\partial z} = -4\pi^2\kappa \csc^2(\pi\beta^2) z - 8\varepsilon\pi\kappa z \csc(\pi\beta^2)$$
$$\times \left(-1 + \cot(\pi\beta^2) - \pi \csc(\pi\beta^2)\right) \qquad (82)$$

Integrating Eqs. (81)–(82) partially with respect to r and z enables us to calculate the total pressure drop. One finds

$$\Delta p = -\frac{\csc^2(\pi\beta^2)}{4r^2} \left[1 + \kappa^2 \left(1 + 8\pi^2 r^2 z^2\right) \right.$$
$$\left. + \kappa^2 \cos(2\pi r^2) + \cos(2\pi\beta^2) \right] - \varepsilon \frac{\kappa \csc(\pi\beta^2)}{2r^2}$$
$$\times \left[\left(\beta^2 \cot(\pi\beta^2) + \csc(\pi\beta^2)\right) \left(1 + 8\pi^2 r^2 z^2 \right.\right.$$
$$\left.\left. - \cos(2\pi r^2)\right) - r^2 \left(8\pi z^2 + \sin(2\pi r^2)\right) \right] \qquad (83)$$

In practice, it must be noted that Eqs. (81) and (83) are virtually insensitive to ε. Being nearly independent of ε, they are well represented by their corresponding curves described by Vyas, Majdalani and Chiaverini[18] for the no wall-injection case. Specifically, they support

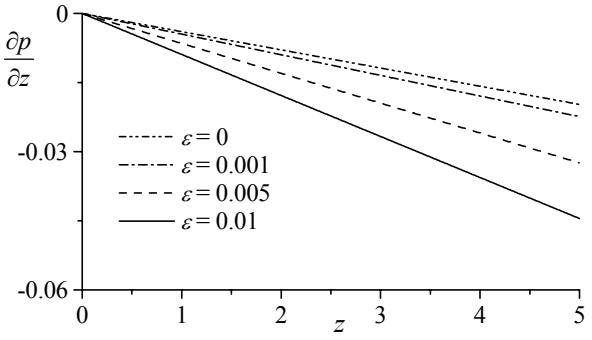

Fig. 6 Axial pressure gradient along the centerline for $\kappa = 0.01$ and several wall injection rates.

the presence of an upward flowing outer vortex. Only the axial pressure gradient is affected by sidewall mass addition as displayed in Fig. 6 where $\partial p/\partial z$ is shown along the chamber centerline. Clearly, the pressure drop in the axial direction is more pronounced when the mass to be driven out of the chamber is increased.

V. Closing Remarks

In this study, a closed-form analytical expression for the hybrid vortex is obtained. The solution emerges from the inviscid Navier-Stokes equations and corroborates the existence of a bipolar, coaxial, vortex pair inside a hybrid chamber model. The current formulation, albeit approximate, exhibits most of the known features of the bidirectional vortex that have been reported in numerical simulations[3,4] or laboratory tests.[5,6] In addition to its ability to predict pressure, velocity, and vorticity distributions throughout the chamber domain, the current solution succinctly captures the movement of the mantle due to variations in regression rate. Our formulation for the hybrid vortex engine supports the existence of a cyclonic flow formation considering that it has been derived from the fundamental equations of motion and a judicious set of boundary conditions. In the interest of clarity, the final solution is summarized in Table 3 for the general case of a nozzle whose diameter matches that of the outflow and in Table 4 for a fixed nozzle diameter corresponding to the no-injection case ($\beta = 1/\sqrt{2}$).

Table 3 Hybrid model for outlet matching inner vortex ($\beta = \beta^*$)

Variable	Two-term approximation
u_r	$-\kappa \csc(\pi\beta^2) r^{-1} \sin(\pi r^2) - \varepsilon \left\{ r^{-1} \sin(\pi r^2) \csc(\pi\beta^2) \times [1 + \beta^2 \cos(\pi\beta^2)] - r \cos(\pi r^2) \right\}$
u_θ	$1/r$
u_z	$\{\pi\kappa \csc(\pi\beta^2) + \pi\varepsilon[1 + \beta^2 \cos(\pi\beta^2)] \csc(\pi\beta^2) - \varepsilon\} \times 2z \cos(\pi r^2) + 2\pi\varepsilon z r^2 \sin(\pi r^2)$
Ω_θ	$4\pi^2 \kappa r z \sin(\pi r^2) \csc(\pi\beta^2) - 4\pi r z \varepsilon \left[\pi r^2 \cos(\pi r^2) + \sin(\pi r^2) \times \left(2 - \pi\beta^2 \cot(\pi\beta^2) - \pi \csc(\pi\beta^2) \right) \right]$
ψ	$\kappa \csc(\pi\beta^2) z \sin(\pi r^2) + \varepsilon \{ [1 + \beta^2 \cos(\pi\beta^2)] \times \csc(\pi\beta^2) z \sin(\pi r^2) - z r^2 \cos(\pi r^2) \}$

Table 4 Hybrid model for fixed outlet radius ($\beta = 1/\sqrt{2}$)

Variable	Two-term approximation
u_r	$-\kappa \sin(\pi r^2)/r + \varepsilon \left[r \cos(\pi r^2) - \sin(\pi r^2)/r \right]$
u_θ	$1/r$
u_z	$2\pi\kappa z \cos(\pi r^2) + 2\varepsilon z \left[(\pi - 1) \cos(\pi r^2) + \pi r^2 \sin(\pi r^2) \right]$
Ω_θ	$4\pi^2 \kappa r z \sin(\pi r^2) + 4\pi r z \varepsilon \left[(\pi - 2) \sin(\pi r^2) - \pi r^2 \cos(\pi r^2) \right]$
ψ	$\kappa z \sin(\pi r^2) + \varepsilon z \left[\sin(\pi r^2) - r^2 \cos(\pi r^2) \right]$

Acknowledgments

This project was sponsored by the Faculty Early Career Development (CAREER) Program of the National Science Foundation under Grant No. CMS-0353518. The authors wish to express their sincere gratitude to the Program Director, Dr. Masayoshi Tomizuka, Dynamic Systems and Control. His genuine interest in this project is greatly appreciated. Additionally, the authors wish to thank all of the program participants who have donated their precious time and passion in promoting the NSF mandate.

References

[1]Casillas, E. D., Shaeffer, C. W., and Trowbridge, J. C., "Cost and Performance Payoffs Inherent in Increased Fuel Regression Rates," AIAA Paper 97-3081, July 6-9 1997.

[2]Knuth, W. H., Bemowski, P. A., Gramer, D. J., Majdalani, J., and Rothbauer, W. J., "Gas-Fed, Vortex Injection Hybrid Rocket Engine," NASA Marshall Space Flight Center, SBIR Phase I Final Technical Rept. NASA/MSFC Contract NAS8-40679, Huntsville, AL, August 1996.

[3]Knuth, W. H., Chiaverini, M. J., Sauer, J. A., and Gramer, D. J., "Solid-Fuel Regression Rate Behavior of Vortex Hybrid Rocket Engines," *Journal of Propulsion & Power,* Vol. 18, No. 3, 2002, pp. 600-609.

[4]Knuth, W. H., Chiaverini, M. J., Gramer, D. J., Sauer, J. A., St. Clair, C. P., Whitesides, R. H., and Dill, R. A., "Preliminary Computational Fluid Dynamics Analysis of the Vortex Hybrid Rocket Chamber and Nozzle Flowfield," AIAA Paper 98-3351, July 1998.

[5]Knuth, W. H., Gramer, D. J., Chiaverini, M. J., and Sauer, J. A., "Development and Testing of Vortex Driven, High Regression Rate Hybrid Rocket Engines," AIAA Paper 98-3507, July 1998.

[6]Knuth, W. H., Chiaverini, M. J., Gramer, D. J., and Sauer, J. A., "Experimental Investigation of a Vortex-Driven High-Regression Rate Hybrid Rocket Engine," AIAA Paper 98-3348, July 1998.

[7]Bloor, M. I. G., and Ingham, D. B., "Theoretical Investigation of the Flow in a Conical Hydrocyclone," *Transactions of the Institution of Chemical Engineers,* Vol. 51, 1973, pp. 36-41.

[8]Bloor, M. I. G., and Ingham, D. B., "The Flow in Industrial Cyclones," *Journal of Fluid Mechanics,* Vol. 178, 1987, pp. 507-519.

[9]Leibovich, S., "Vortex Stability and Breakdown: Survey and Extension," *AIAA Journal,* Vol. 22, No. 9, 1984, pp. 1192-1206.

[10]Leibovich, S., "The Structure of Vortex Breakdown," *Annual Review of Fluid Mechanics*, Vol. 101978, pp. 221-246.

[11]Beran, P. S., and Culick, F. E. C., "The Role of Non-Uniqueness in the Development of Vortex Breakdown in Tubes," *Journal of Fluid Mechanics,* Vol. 242, 1992, pp. 491-527.

[12]Vatistas, G. H., Lin, S., and Kwok, C. K., "Reverse Flow Radius in Vortex Chambers," *AIAA Journal,* Vol. 24, No. 11, 1986, pp. 1872-1873.

[13]Vatistas, G. H., Lin, S., and Kwok, C. K., "Theoretical and Experimental Studies on Vortex Chamber Flows," *AIAA Journal,* Vol. 24, No. 4, 1986, pp. 635-642.

[14]Szeri, A., and Holmes, P., "Nonlinear Stability of Axisymmetric Swirling Flows," *Philosophical Transactions of the Royal Society of London, Series A,* Vol. 326, 1988, pp. 327-354.

[15]Gupta, A. K., Lilley, D. G., and Syred, N., *Swirl Flows*, Abacus, Turnbridge Wells, UK, 1984.

[16]Hoekstra, A. J., Derksen, J. J., and Van den Akker, H. E. A., "An Experimental and Numerical Study of Turbulent Swirling Flow in Gas Cyclones," *Chemical Engineering Science,* Vol. 54, 1999, pp. 2055-2065.

[17]Culick, F. E. C., "Rotational Axisymmetric Mean Flow and Damping of Acoustic Waves in a Solid Propellant Rocket," *AIAA Journal,* Vol. 4, No. 8, 1966, pp. 1462-1464.

[18]Vyas, A. B., Majdalani, J., and Chiaverini, M. J., "The Bidirectional Vortex. Part 1: An Exact Inviscid Solution," AIAA Paper 2003-5052, July 2003.

[19]Majdalani, J., Vyas, A. B., and Flandro, G. A., "Higher Mean-Flow Approximation for a Solid Rocket Motor with Radially Regressing Walls," *AIAA Journal,* Vol. 40, No. 9, 2002, pp. 1780-1788.

[20]Zhou, C., and Majdalani, J., "Improved Mean Flow Solution for Slab Rocket Motors with Regressing Walls," *Journal of Propulsion and Power,* Vol. 18, No. 3, 2002, pp. 703-711.

[21]Wolfram, S., Mathematica. A System for Doing Mathematics on Computer. Addison Wesley, Reading, MA, 1988.

[22]Chiaverini, M. J., Serin, N., Johnson, D. K., Lu, Y.-C., Kuo, K. K., and Risha, G. A., "Regression Rate Behavior of Hybrid Rocket Solid Fuels," *Journal of Propulsion and Power,* Vol. 16, No. 1, 2000, pp. 125-132.